Draft version December 5, 2025
Typeset using LaTeX **twocolumn** style in AASTeX631

Statistical and Temporal Analysis of Multi-component Burst-clusters from the Repeating FRB 20190520B

Jia-heng Zhang [1,2,3] Chen-Hui Niu* [1,2,3] Yu-hao Zhu [4,5] Di Li [6,4,7] Yu Wang,[8] Wei-yang Wang [5] Yi Feng,[7,9] Xin-ming Li [1,2,3] Jia-rui Niu [4] Pei Wang [4] Yun-wei Yu [1,2,3] Yong-kun Zhang [4] and Xiao-ping Zheng[1,2,3]

[1] Institute of Astrophysics, Central China Normal University, Wuhan 430079, China
[2] Education Research and Application Center, National Astronomical Data Center, Wuhan 430079, China
[3] Key Laboratory of Quark and Lepton Physics (Central China Normal University), Ministry of Education, Wuhan 430079, China
[4] National Astronomical Observatories, Chinese Academy of Sciences, Beijing 100101, China
[5] School of Astronomy and Space Science, University of Chinese Academy of Sciences, Beijing 100049, China
[6] Department of Astronomy, Tsinghua University, Beijing 100084, China
[7] Research Center for Astronomical Computing, Zhejiang Laboratory, Hangzhou 311100, China
[8] ICRANet, Piazza della Repubblica 10, 65122 Pescara, Italy
[9] Institute for Astronomy, School of Physics, Zhejiang University, Hangzhou 310027, China

ABSTRACT

Fast Radio Bursts (FRBs) are bright, millisecond-duration extragalactic radio transients that probe extreme astrophysical environments. Many FRBs exhibit multi-component structures, which encode information about their emission mechanisms or progenitor systems and thus provide important clues to their origins. In this work, we systematically analyze the burst morphology of FRB 20190520B and compare component distributions across four active FRBs observed with FAST: FRB 20121102A, FRB 20190520B, FRB 20201124A, and FRB 20240114A. We find that multi-component burst-clusters show spectral properties similar to single-peak bursts, and no periodicity is detected in their temporal behavior. The component-count distributions follow a power law, revealing scale-free behavior consistent with self-organized criticality (SOC) processes. Multi-component clusters account for 12–30% of all detected bursts, regardless of source activity, providing new insights into burst-to-burst variability and the physical processes driving FRB emission.

Keywords: Fast radio burst, multi-component, FRB 20190520B, SOC

1. INTRODUCTION

Fast Radio Bursts (FRBs) are high-energy astrophysical phenomena characterized by short, intense bursts of radio emission lasting only milliseconds. Since their discovery in 2007 (Lorimer et al. 2007), FRBs have posed significant challenges to our understanding of the astrophysics of compact objects. Many of these bursts exhibit high dispersion measures (DMs) that exceed the predictions of Galactic electron density models along their lines of sight (Cordes 2004; Yao et al. 2017), suggesting an extragalactic origin (Cordes & Chatterjee 2019; Zhang 2020; Petroff et al. 2022). A major breakthrough came with the identification of the first repeating source, FRB 20121102A, in 2016 (Spitler et al. 2016), which opened up unprecedented opportunities for follow-up studies. To date, over 800 FRB sources have been discovered, with roughly 10% of them exhibiting repeating behavior[1]. A subset of these have also been localized to host galaxies. In contrast to one-off FRBs, repeating FRBs offer a unique window into the underlying physical mechanisms and local environments of FRB sources (CHIME/FRB Collaboration et al. 2019; Fonseca et al. 2020; CHIME/FRB Collaboration et al. 2021).

Multi-component structures in radio emission were firstly discovered in pulsars (Craft et al. 1968), and were subsequently analyzed in FRB 20121102A (Hessels et al.

niuchenhui@ccnu.edu.cn

[1] https://blinkverse.zero2x.org

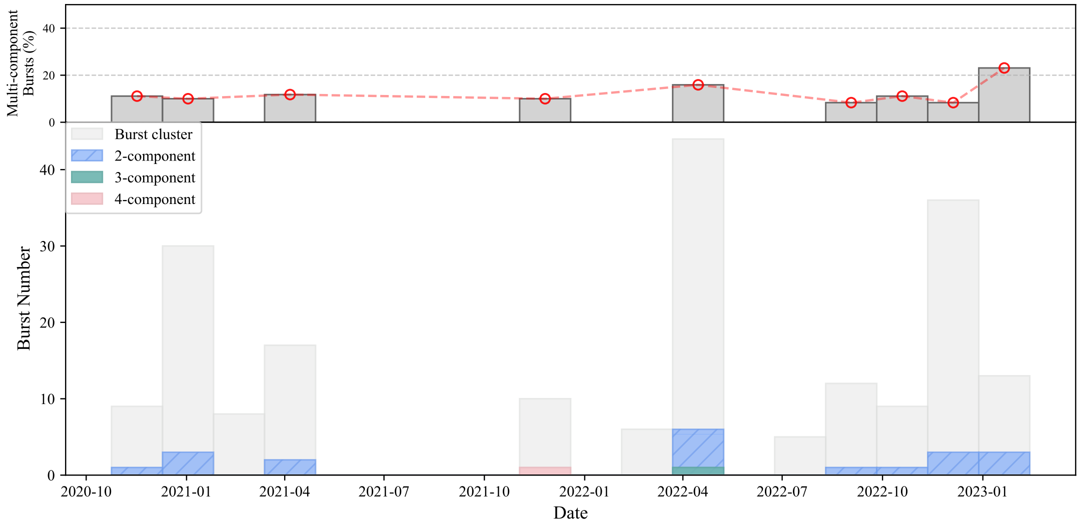

Figure 1. The horizontal axis represents the dates, and the vertical axis shows the number of bursts. Different colors are used to distinguish the total burst count, bimodal burst structure, trimodal burst structure, and quadrimodal burst structure.

2019). Since then, such features have been observed in multiple FRB sources, characterized by complex multi-component structures and quasi-periodic patterns (Zhou et al. 2022; Pastor-Marazuela et al. 2023; Niu J.-R. et al. 2022; Majid et al. 2021; Kramer et al. 2024). The presence of these multi-component structures in FRBs has drawn a close analogy between FRBs and pulsars. Moreover, the temporal and spectral evolution of these fine structures may offer further insights into the underlying radiation mechanisms.

The periodicity of FRB multi-component structure has also been studied. In FRB 20201124A, a broad distribution of sub-burst separations around 5 ms was reported (Niu J.-R. et al. 2022), but without a consistent or dominant period, suggesting an origin in intrinsic radiation processes rather than rotational modulation. A tentative 1.7-second periodicity was observed in FRB 20201124A on two isolated days, potentially linked to magnetar rotation(Du et al. 2025), though its sporadic appearance leaves the origin uncertain. Similar quasi-periodic features have also been observed across a range of timescales. FRB 20201020A exhibits a quasi-periodic structure with five subcomponents regularly spaced by 0.411 ms, suggesting a potential magnetospheric origin for such periodicity (Pastor-Marazuela et al. 2023). Kramer et al. (2024) reported that the quasi-periodic sub-structures seen in pulsar and magnetar radio emission scale with their rotational periods, suggesting a possible link between multi-component structures timescales and the spin of the neutron star. If FRBs originate from similar systems, such scaling could in principle be used to infer their underlying periods. However, no direct observational evidence has confirmed the validity of this relationship in FRBs to date.

One of the most intriguing repeating sources, FRB 20190520B, was discovered by the Five-hundred-meter Aperture Spherical Radio Telescope (FAST) and is co-located with a compact, luminous persistent radio source (PRS) in a star-forming dwarf galaxy at redshift z = 0.241 (Niu C.-H. et al. 2022). This source exhibits a high repetition rate, complex burst morphology with multi-component structures, and an exceptionally large DM of $1204.7\pm4.0\,\mathrm{pc\,cm^{-3}}$, of which $\sim 903^{+72}_{-111}\,\mathrm{pc\,cm^{-3}}$ is attributed to the host galaxy. This host DM far exceeds that of other known FRBs and deviates significantly from the Macquart relation (Macquart et al. 2020), implying that a substantial fraction of the dispersion originates in its local environment rather than in the intergalactic medium. The persistent radio counterpart has a luminosity of $\sim 3\times10^{29}\,\mathrm{erg\,s^{-1}\,Hz^{-1}}$, and its compactness and brightness closely resemble those of FRB 20121102A. These similarities suggest that FRB 20190520B and FRB 20121102A may represent a distinct subclass of young repeating FRBs embedded in dense magneto-ionic environments, making FRB 20190520B an ideal laboratory for studying the interplay between FRB emission and its local environment.

In this paper, we focus on the overall morphological characteristics of multi-component FRB bursts of FRB 20190520B, analyzing their time-frequency behavior, spectral distribution, and the statistical properties of component counts. We choose FRB 20190520B as our target because its sustained activity allows continuous monitoring on yearly timescales, and its bursts often

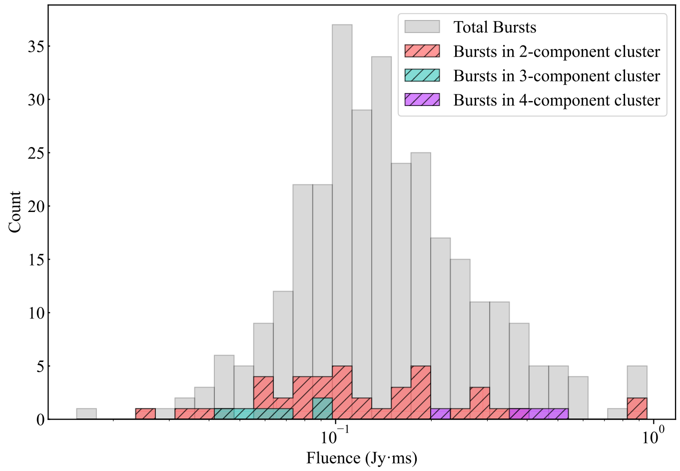

Figure 2. Distribution of burst fluences detected from FRB 20190520B. The horizontal axis represents the fluence (Jy·ms), and the vertical axis shows the burst count. The gray bars denote the total distribution of all bursts, while the hatched colored bars highlight bursts that belong to multi-component structures: red for bursts in 2-component clusters, cyan for bursts in 3-component clusters, and purple for bursts in 4-component clusters.

exhibit rich multi-component structures that are ideal for statistical investigation. By statistically examining a large sample of bursts from a repeating source, we aim to provide a refined understanding of the emission structure and its physical implications. Sections 2 and 3 describe our observations, burst detection, and data reduction procedures, including flux calibration. Section 4 presents the analysis of multi-component burst-clusters, focusing on their time–frequency behavior, spectral features, and temporal properties. Section 5 summarizes the main results, compares the component count statistics of FRB 20190520B with those of other repeating FRB sources. Section 6 provides a discussion of the results and the overall conclusions.

2. OBSERVATIONS

FRB 20190520B was observed with the Five-hundred-meter Aperture Spherical Radio Telescope (FAST), using the central beam of the 19-beam L-band receiver and the pulsar backend. The system covered the frequency range 1.0–1.5 GHz (centered at 1.25 GHz) with a time resolution of 49.152 μs and a frequency resolution of 0.122 MHz. The data were recorded in the standard PSRFITS with full-Stokes polarization information.

The observations and search procedures are identical to those described in Niu C.-H. et al. (2022) and Niu et al. (2025), and we summarize them here for completeness. Candidate bursts were identified with the HEIMDALL pipeline (Barsdell et al. 2012), applying a zero-DM matched filter for RFI excision. Events with S/N > 7 were visually inspected using their dynamic spectra to confirm astrophysical origin.

Flux calibration was carried out following the standard procedure inNiu et al. (2025), using an injected periodic noise signal with a known reference temperature before each observation. From the calibrated data, we derived the burst properties including DM, temporal width, center frequency, bandwidth, peak flux density, fluence, and isotropic-equivalent energy (Zhang 2018; Gourdji et al. 2019).

From October 24, 2020, to April 1, 2023, a total of 72 observing sessions were conducted, corresponding to 72.04 hours of on-source time. In this new search (Niu et al. 2025), 360 bursts were detected. The burst parameters were uniformly measured and compiled into a catalog, which serves as the basis for the statistical analyses presented in the following sections. The average event rate across all sessions was approximately 5.0 bursts per hour.

3. DATA

In this section, we present the criteria used to identify burst-clusters in our dataset and describe the characteristics of the bursts within them. Following Zhou

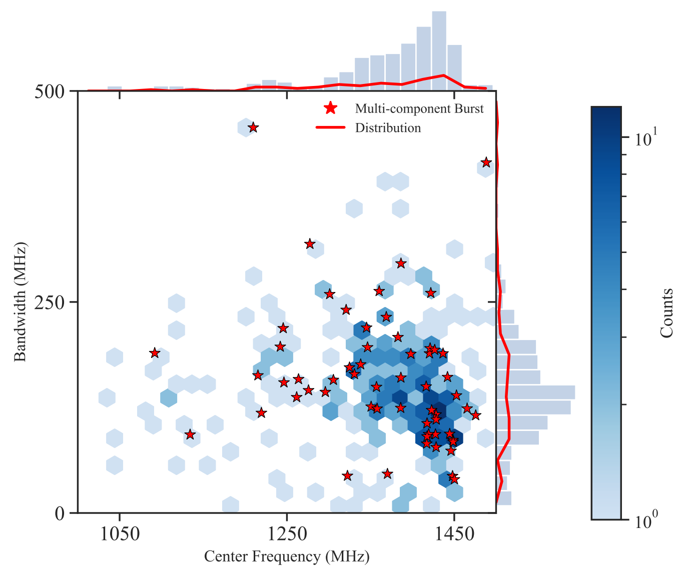

Figure 3. Distribution of burst center frequencies and bandwidths for FRB 20190520B. The blue hexagons represent all detected bursts, with the color intensity indicating the number of bursts in each bin. Red stars mark bursts that belong to multi-component burst-clusters. The marginal histograms along the top and right axes show the overall distributions of burst center frequency and bandwidth, respectively. The red curve represents the distribution of the multi-component burst-clusters (red stars) in center frequency and bandwidth.

et al. (2022) and Zhang et al. (2025), we define a *burst-cluster* as a collection of bursts (excluding those labeled as "Not-Clear") in which the time separations between adjacent components (or peaks) are shorter than a threshold τ. The threshold τ is determined from the valley in the bimodal waiting-time distribution; for example, Zhang J.-S. et al. (2025) derived $\tau = 400$ ms for FRB 20240114A (see their Extended Data Figure 2). A single burst is still classified as a burst-cluster if no other bursts are detected within the τ-duration intervals immediately preceding and following it.

While Zhou et al. (2022) and Zhang et al. (2025) further distinguish between *sub-bursts* (quasi-connected components with visually separable peaks in the dedispersed profile) and *bursts* (groups of such sub-bursts), in this work we do not make this distinction. For convenience in our multi-component structure analysis, we refer to any individual component within a burst-cluster as a *burst*, provided that the difference between its peak and the adjacent valley exceeds 3σ above the baseline noise level. This simplified definition enables a consistent treatment of both single-component and multi-component structures, while remaining compatible with the more detailed hierarchical definitions presented in the literature.

Applying the above criteria to our dataset yields 315 burst-clusters containing a total of 360 bursts. The waiting time distribution of FRB 20190520B is shown in Appendix Figure A1. Among these burst-clusters, 12.06% display clear multi-component temporal profiles. Furthermore, 38 burst-clusters exhibit waiting times shorter than 123.8 ms, of which 34 consist of two peaks, three contain three peaks, and one features four adjacent peaks. To illustrate the fraction of multi-component structures among the total detected bursts, we imposed a threshold of at least five bursts per observing session; sessions with fewer than five bursts were excluded due to the relatively low burst rate of FRB 20190520B. After this filtering, we obtained Figure 1. The bin size was chosen to be 50 days so as to ensure that each bin typically contains data from more than two observing sessions. Different colors represent bursts with different numbers of components. As shown, the fraction of multi-component burst-clusters remains at or below the 20% level when calculated with a bin size of 50 days.

4. ANALYSIS

In this section, we analyze the multi-component structures of FRB 20190520B through various aspects, including fluence and spectral analysis, as well as temporal analysis. We first examine the fluence distribution and spectral properties of the detected bursts, followed by a detailed temporal analysis of multi-component burst-clusters. Using the Lomb-Scargle (LS) period search method, we identify potential periodicities in the burst profiles. Additionally, we apply linear fitting techniques to determine the time of arrival (TOA) of each subcomponent and assess the confidence of detected periodicities.

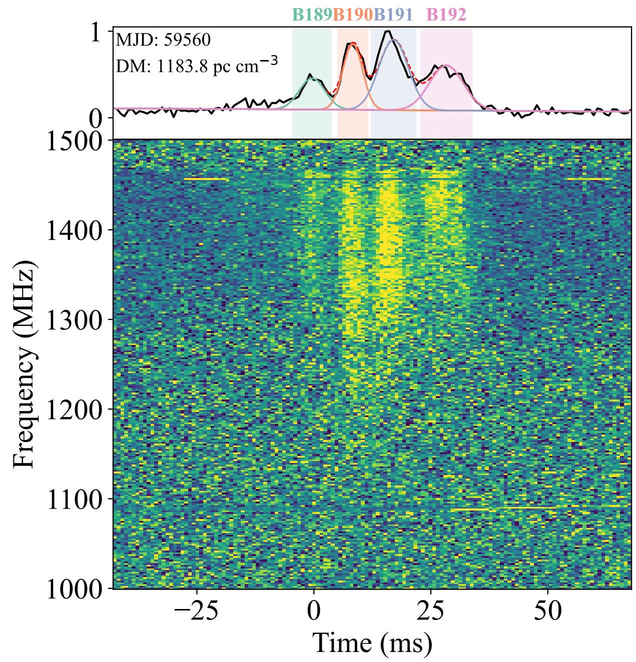

Figure 4. Two-dimensional dynamic spectrum of a 4-component burst. Top panel: The average pulse profile, with the burst MJD and the measured DM value both annotated in the upper left corner. Multiple Gaussian functions were fitted to the profile using curves of different colors, and the corresponding components are marked with the same colors. **Bottom panel**: The waterfall plot of signal intensity (dynamic spectrum).

4.1. *Fluence and Spectral Properties*

Figure 2 shows the fluence distribution of the 316 detected bursts, after excluding 44 bursts that could not be energy-calibrated because no known-temperature noise signal was injected during those observations. From the figure, the fluence of multi-component burst-clusters does not appear to be more concentrated in any particular region, but rather tends to be consistent with the overall fluence distribution of all bursts.

FRB 20190520B is a high-frequency, narrow-band source, with most bursts occurring near 1.4 GHz and exhibiting relatively narrow bandwidths in FAST observations(Zhu et al. 2024). As shown in Figure 3, the majority of bursts cluster around a center frequency of 1429.3 ± 6.9 MHz and a bandwidth of 112.1 ± 8.6 MHz. Multi-component burst-clusters, indicated by red pentagram markers, occupy a similar region in the frequency–bandwidth plane, suggesting that their spectral characteristics are broadly consistent with those of the full burst population. Statistical analysis, including the Kolmogorov–Smirnov (K-S) test and Mann–Whitney U test, confirms that neither the fluence distributions ($p > 0.05$ in both tests) (Kolmogorov 1933; Smirnov 1948; Mann & Whitney 1947) nor the center frequency and bandwidth distributions (K-S: $p = 0.521$; Mann–Whitney U: $p = 0.685$) of multi-component burst-clusters differ significantly from those of the overall burst sample, supporting the conclusion that their fluence and spectral properties are consistent with the general burst population.

4.2. *Temporal Analysis of Multi-component Burst-clusters*

In previous studies, periodicity searches of multi-component structures have been considered highly important. In Niu J.-R. et al. (2022), the periodicities of multi-component burst-clusters from FRB 20201124A were systematically analyzed, and a distribution of characteristic periods was obtained. Kramer et al. (2024) further suggested that such periodicities might be related to the rotational period of the source. Motivated by these results, we performed a periodicity search for the multi-component structures of FRB 20190520B. Since meaningful periodicity searches can only be conducted for bursts with at least three components, we applied two methods to one 4-component burst and three 3-component bursts in our dataset. Figure 4 presents the 4-component burst-cluster. The top panel shows the burst profile, where we fitted multiple Gaussian functions to identify each component, highlighted with different colors. The bottom panel displays the corresponding waterfall plot of the same burst-cluster. The periodicity analysis for this 4-component burst-cluster is shown in Figure 5, while the results for the 3-component bursts are provided in the Appendix Figure A2 and Appendix Figure A3).

4.2.1. *Lomb–Scargle Periodicity Search*

Compared to traditional Fourier transform techniques, the LS method is more effective for irregularly sampled data and is particularly useful in extracting significant periodic signals from pulse profiles.The LS method has become a widely adopted tool for period analysis.

We processed the data of the 4-component burst-cluster as follows. First, the signals across all frequency channels were averaged (after correcting for the dispersion measure and removing RFI contamination) to obtain the time-domain pulse profile. This profile was then normalized to yield a one-dimensional time series. We applied the LS algorithm to this series, where the searched periods depend on both the length of the time series and the number of trial periods. For this analysis, we restricted the search range to 1–30 ms. As shown in panel (a) of Figure 5, the LS power spectrum of a representative burst with four distinct subcomponents exhibits a prominent peak at $P = 8.200^{+0.686}_{-0.568}$ ms, with additional peaks corresponding to harmonic multiples of the fundamental period. The quoted asymmetric uncertainties are derived from the full width at half maximum (FWHM) of the main peak.

To assess the statistical significance of this result, we generated 10^6 synthetic noise profiles based on the original pulse time series. For each realization, we computed the LS power at the period where the original profile exhibited its highest LS power. The significance was evaluated by comparing the distribution of these LS powers with the observed peak power in the original data. The result, corresponding to a confidence level of about 2.3 σ, is shown in panel (b) of Figure 5.

4.2.2. *Linear Fitting of Sub-pulse Arrival Times (TOA) for Period Determination*

As previously outlined, Andersen et al. (2022) introduced a method to determine periodicity by extracting the time of arrival (TOA) of each subcomponent via multi-Gaussian fitting. These TOAs are then fitted linearly using the following model:

$$t_i = \bar{d} n_i + T_0, \tag{1}$$

where t_i represents the TOA of the i-th subcomponent, $\bar{d}$ denotes the average spacing between subcomponents within a single burst (which corresponds to the target period P), n_i is the index of the i-th subcomponent, and T_0 is the TOA of the first component. The result of this linear fit, shown in panel (c) of Figure 5, yields a periodicity of $P = 9.03 \pm 0.56$ ms.

To evaluate the robustness of the detected periodicity, we generated the subcomponent spacings d_i from a shifted–exponential law (i.e., a Poisson-process interarrival distribution with a deterministic offset),

$$d_i = \bar{d}\left[\eta - (1-\eta)\ln(1-u_i)\right], \qquad u_i \sim \mathcal{U}(0,1), \tag{2}$$

with shift fraction $\eta = 0.2$ following Pastor-Marazuela et al. (2023). For each simulated sample, we computed the reduced chi-squared ($\chi^2_{\rm red}$) and assessed significance by comparing the observed $\chi^2_{\rm red}$ against the simulation distribution. The observed periodicity corresponds to

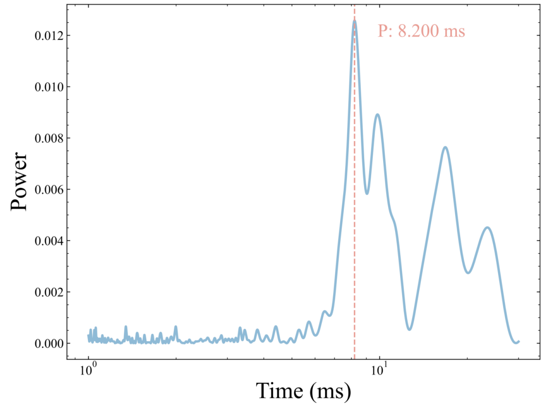

(a)

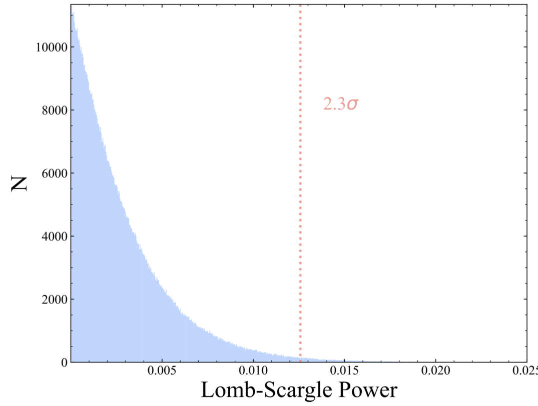

(b)

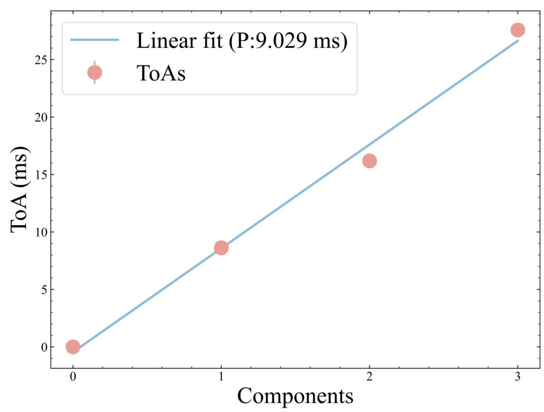

(c)

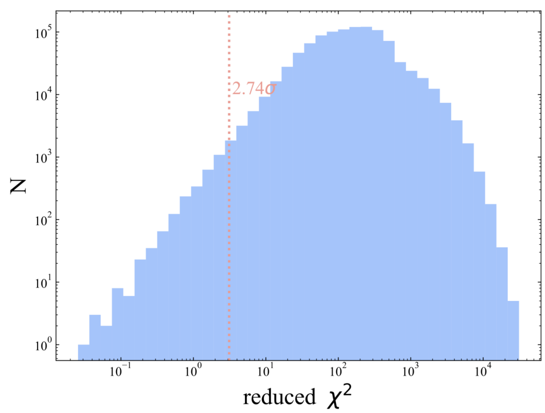

(d)

Figure 5. Temporal analysis of the 4-component burst. **(a)** Lomb–Scargle periodogram of the four-component burst. The horizontal axis represents the trial periods T (in milliseconds) scanned during the search, while the vertical axis shows the Lomb–Scargle power. The red dashed line indicates the period at which the power reaches its maximum, corresponding to the most significant periodicity. **(b)** Distribution of LS powers obtained from 10^6 randomly generated noise time series. The horizontal axis shows the LS power, and the vertical axis gives the occurrence count N. The red dashed line marks the LS power measured from the real burst data, corresponding to a significance level of 2.3σ. **(c)** Linear fit of times of arrival (TOAs). The horizontal axis represents the component number in the multi-component structure, while the vertical axis shows the TOAs (ms). The red points are the TOAs derived from Gaussian fits to each peak, and the blue line is the linear fit, yielding the corresponding periodicity. **(d)** Significance test of the linear fit. The figure shows the distribution of reduced χ^2 values obtained from 10^6 random trials, where random time stamps were generated and compared with the previously derived linear fit to compute the reduced χ^2. The red dashed line marks the reduced χ^2 value from the real data, corresponding to a confidence level of 2.74σ.

a confidence level of 2.74σ, as shown in panel (d) of Figure 5.

5. RESULTS

In this study, we analyzed the fluence, spectral, and temporal properties of multi-component burst-clusters in the FRB 20190520B dataset. We find that the fluence and spectral distributions of the bursts in multi-component burst-clusters are statistically consistent with the overall burst population, while temporal analyses using LS periodograms and linear fitting of sub-pulse TOAs reveal candidate periodicities in bursts with three or more components, with their significance evaluated through extensive noise simulations. The temporal analyses of the other three-component burst-clusters also yield corresponding quasi-periodicities. However, no clear correlation is found among these periods, which is consistent with the results of Niu J.-R. et al. (2022) for the multi-component burst-clusters of FRB 20201124A.

We attempted to connect the periodicities obtained from the multi-component burst-clusters with the intrinsic rotation period of the source (Kramer et al. 2024). Using the relation $P_\mu = (0.94 \pm 0.04) \times P^{(+0.97\pm0.05)}$ ms, we derived the corresponding rotation period and performed phase-folding of the time series. However, this approach did not yield satisfactory results. Further-

Table 1. Statistics of multi-component burst-clusters from selected FRB sources

FRB Source	Total burst-clusters	Multi-component Burst-clusters (≥2)	Fraction	Burst Rate (h^{-1})
FRB 20190520B	315	38	12.06%	5
FRB 20201124A	604	186	30.79%	46.5
FRB 20121102A	1312	292	22.26%	27.7
FRB 20240114A	8778	1858	21.17%	333

more, when we directly folded the TOAs sequence of all 360 bursts using the periodicities inferred from the multi-component burst-clusters, no evidence of a significant periodic signal was found.

To quantify and compare the multiplicity of emission within clusters across active repeating FRBs, we focus on four well-studied sources: FRB 20121102A (Li et al. 2021), FRB 20190520B (this work), FRB 20240114A (Zhang J.-S. et al. 2025), and FRB 20201124A (Zhang et al. 2022). For consistency, we adopt unified working definitions: a *burst-cluster* is defined by a maximum intra-cluster time separation set by the valley between the two peaks of the bimodal waiting-time distribution (following previous studies), while an individual *burst* within a cluster is identified as a component whose peak-to-valley flux contrast exceeds 3σ above the baseline noise level, consistent with Section 3. The waiting-time distribution used for this definition is shown in Figure A1.

Table 1 summarizes the statistics of multi-component burst-clusters for the four repeating FRBs analyzed in this work. In addition, Figure 7 presents the fractions of multi-component structures and the corresponding burst rates for each source. FRB 20190520B shows a total of 315 burst-clusters, of which only 38 exhibit multiple components, corresponding to a fraction of 12.06% and the lowest burst rate among the four sources. In contrast, FRB 20201124A, FRB 20121102A, and FRB 20240114A display substantially higher fractions of multi-component burst-clusters, at 30.79%, 22.26%, and 21.17%, respectively. Notably, FRB 20201124A has the highest fraction of multi-component burst-clusters, but without the highest burst rate. This indicates that the burst rate and the fraction of multi-component structures are not necessarily correlated.

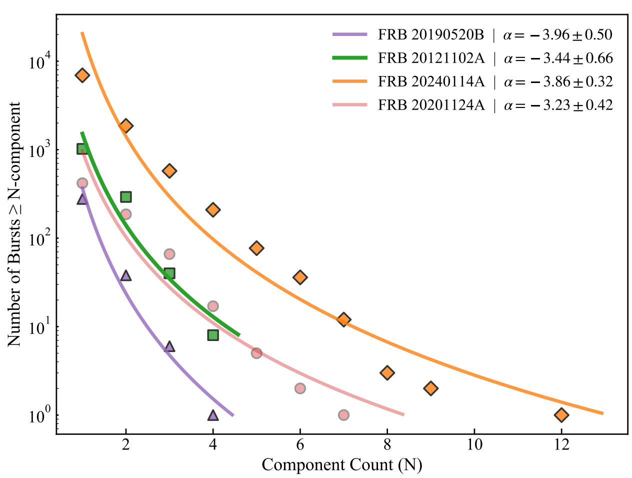

Figure 6. Cumulative distribution of burst-clusters as a function of the number of components (n) per cluster for FRB 20190520B and other repeating FRB sources. The vertical axis shows the number of clusters with n or more components, and the horizontal axis represents n.

Pastor-Marazuela et al. (2025) reported that 7 out of 24 one-off FRBs in their Apertif sample (∼30%) exhibit multi-component temporal structures. At the same time, they also re-examined 130 one-off FRBs from the First CHIME/FRB Catalog and found that about 28% display complex, multi-component morphologies. These comparable fractions suggest that the occurrence of multi components is not uncommon even among apparently one-off FRBs. The authors further argued that such complexity may reflect an intrinsic property of FRB emission, in close analogy with pulsars, whose profiles frequently show multi-component structures as a consequence of their underlying radiation mechanisms.

For each source, we construct the cumulative distribution of component counts per cluster, plotting $N_{\rm bursts}(\geq N)$ versus N in semi–log space and fitting power-law models $N_{\rm bursts}(\geq N) \propto N^{-\alpha}$ (slopes listed in the legend of Figure 6). The fitting was performed by ordinary least-squares regression in semi–log space, with best-fit parameters and 1σ uncertainties derived from the covariance matrix. The power-law distribution indicates a scale-free behavior in the burst emission. Such a scale-free distribution suggests that there is no characteristic number of sub-pulses, with both small and large sub-pulse clusters arising from the same underlying process. This behavior is naturally consistent with a self-organized criticality (SOC) scenario, where the FRB source evolves toward a critical state rather than being governed by purely random or Poissonian processes.

FRB 20190520B and FRB 20121102A exhibit steeper slopes, indicating that clusters with large N are comparatively rare, whereas FRB 20240114A and FRB 20201124A show shallower slopes, implying a higher fraction of clusters with multiple components. These contrasting behaviors may reflect intrinsic differences in emission mechanisms or source environments among repeaters. In principle, a single trigger event can launch multiple particle beams propagating along different magnetic field lines; however, the geometry dictated by the magnetospheric configuration and the star's rotation prevents not all resulting FRB beams from crossing the observer's line of sight, which causes the sub-pulses to exhibit identical statistical properties (Wang et al. 2019).

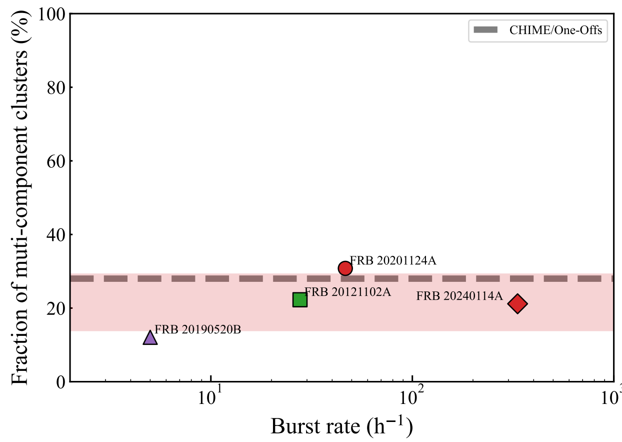

Figure 7. Relation between the burst rate and the fraction of multi-component burst-clusters for different FRB sources. Different colors and marker shapes denote different FRB sources. The red-shaded area marks the range of the fraction. The gray dashed line represents the CHIME result from visual re-examination reported by Pastor-Marazuela et al. (2025), corresponding to a fraction of about 28%.

6. DISCUSSION AND CONCLUSION

In this work, we carried out a systematic investigation of the multi-component burst-clusters from FRB 20190520B using high-sensitivity FAST observations. Our fluence and spectral analyses show that multi-component clusters share broadly similar properties with single-component bursts, with no significant differences in flux density distribution, center frequency, or bandwidth. These results indicate that the occurrence of multi-component structures is not driven by distinct emission energetics or spectral characteristics, but instead arises from temporal modulation within the same underlying emission process.

The temporal analysis further reveals that several bursts exhibit quasi-periodic sub-structures on millisecond timescales. By applying both Lomb–Scargle periodograms and linear fits to sub-pulse times of arrival, we identified multiple distinct quasi-periodicities within the multi-component structures. Multi-component structures are observed to occur sporadically and exhibit variations from burst to burst, in agreement with previous studies of other FRBs. This behavior suggests that such fine-scale structures are more likely linked to intrinsic magnetospheric emission processes. However, no corresponding spin period can be established across the overall sample.

Building on these results, we carried out a broader comparison across different repeating FRBs. Our comparative analysis of multi-component burst-clusters highlights several key results. First, FRB 20190520B exhibits a markedly lower fraction of multi-component clusters ($\sim$12%) compared to other active repeaters such as FRB 20201124A, FRB 20121102A, and FRB 20240114A. Second, we find no evidence for a correlation between the overall burst rate and the fraction of multi-component structures, suggesting that the emergence of such complexity is governed primarily by intrinsic emission processes rather than the global activity level.

Third, comparisons with one-off FRBs [2]reveal that $\sim$30% also display multi-component structures, implying that such morphologies are not unique to repeaters but may reflect a more fundamental property of FRB emission, analogous to the multi-component profiles seen in pulsars. Finally, the cumulative distribution of component counts follows a power-law form, pointing toward a scale-free behavior such as SOC. This finding challenges purely random interpretations and links FRBs to a broader class of astrophysical SOC phenomena, such as solar flares and starquakes, thereby offering new physical perspectives on FRB mechanisms.

Future progress will benefit from larger samples of multi-component burst-clusters across different repeaters, as well as higher time-resolution observations that can better resolve microsecond-level structures. In particular, polarimetric and wideband studies may reveal whether the temporal regularity observed in some bursts is accompanied by correlated changes in polarization or frequency drift. Combining such analyses with theoretical modeling of magnetospheric plasma processes will be crucial to uncover the physical origin of FRB multi-component structure.

[2] There is ongoing debate on whether all FRBs are capable of repetition with widely varying activity rates (Ravi 2019; Kirsten et al. 2024; Yamasaki et al. 2024).

ACKNOWLEDGMENTS

This work was supported by the National Natural Science Foundation of China (NSFC) under Programs No. 11988101 and 12203069. C.H.N. acknowledges support from the National SKA Program of China (2022SKA0130100), the Basic Research Project of Central China Normal University, and the Hubei QB Project. C.H.N. also thanks the CAS Youth Interdisciplinary Team and the Foundation of Guizhou Provincial Education Department for Grant No. KY(2023)059.

This work made use of data from FAST (Five-hundred-meter Aperture Spherical Radio Telescope). We thank the FAST data center operations team for scheduling the follow-up observations and facilitating data acquisition.

REFERENCES

Andersen, B. C., Bandura, K., Bhardwaj, M., et al. 2022, Nature, 607, 256, doi: 10.1038/s41586-022-04841-8

Barsdell, B. R., Bailes, M., Barnes, D. G., & Fluke, C. J. 2012, MNRAS, 422, 379, doi: 10.1111/j.1365-2966.2012.20622.x

CHIME/FRB Collaboration, Andersen, B. C., Bandura, K., et al. 2019, ApJL, 885, L24, doi: 10.3847/2041-8213/ab4a80

CHIME/FRB Collaboration, Amiri, M., Andersen, B. C., et al. 2021, ApJS, 257, 59, doi: 10.3847/1538-4365/ac33ab

Cordes, J. M. 2004, in Astronomical Society of the Pacific Conference Series, Vol. 317, Milky Way Surveys: The Structure and Evolution of our Galaxy, ed. D. Clemens, R. Shah, & T. Brainerd, 211

Cordes, J. M., & Chatterjee, S. 2019, ARA&A, 57, 417, doi: 10.1146/annurev-astro-091918-104501

Craft, H. D., Comella, J. M., & Drake, F. D. 1968, Nature, 218, 1122, doi: 10.1038/2181122a0

Du, C., Huang, Y.-F., Geng, J.-J., et al. 2025, arXiv e-prints, arXiv:2503.12013, doi: 10.48550/arXiv.2503.12013

Fonseca, E., Andersen, B. C., Bhardwaj, M., et al. 2020, ApJL, 891, L6, doi: 10.3847/2041-8213/ab7208

Gourdji, K., Michilli, D., Spitler, L. G., et al. 2019, ApJL, 877, L19, doi: 10.3847/2041-8213/ab1f8a

Hessels, J. W. T., Spitler, L. G., Seymour, A. D., et al. 2019, ApJL, 876, L23, doi: 10.3847/2041-8213/ab13ae

Kirsten, F., Ould-Boukattine, O. S., Herrmann, W., et al. 2024, Nature Astronomy, 8, 337, doi: 10.1038/s41550-023-02153-z

Kolmogorov, A. N. 1933, Giornale dell'Istituto Italiano degli Attuari, 4, 83

Kramer, M., Liu, K., Desvignes, G., Karuppusamy, R., & Stappers, B. W. 2024, Nature Astronomy, 8, 230, doi: 10.1038/s41550-023-02125-3

Li, D., Wang, P., Zhu, W. W., et al. 2021, Nature, 598, 267, doi: 10.1038/s41586-021-03878-5

Lorimer, D. R., Bailes, M., McLaughlin, M. A., Narkevic, D. J., & Crawford, F. 2007, Science, 318, 777, doi: 10.1126/science.1147532

Macquart, J. P., Prochaska, J. X., McQuinn, M., et al. 2020, Nature, 581, 391, doi: 10.1038/s41586-020-2300-2

Majid, W. A., Pearlman, A. B., Prince, T. A., et al. 2021, ApJL, 919, L6, doi: 10.3847/2041-8213/ac1921

Mann, H. B., & Whitney, D. R. 1947, Annals of Mathematical Statistics, 18, 50

Niu, C.-H., Li, D., Yang, Y.-P., et al. 2025, Science Bulletin, doi: https://doi.org/10.1016/j.scib.2025.11.023

Niu C.-H., and Aggarwal, K., Li, D., Zhang, X., et al. 2022, Nature, 606, 873, doi: 10.1038/s41586-022-04755-5

Niu J.-R., J.-R., Zhu, W.-W., Zhang, B., et al. 2022, Research in Astronomy and Astrophysics, 22, 124004, doi: 10.1088/1674-4527/ac995d

Pastor-Marazuela, I., van Leeuwen, J., Bilous, A., et al. 2023, A&A, 678, A149, doi: 10.1051/0004-6361/202243339

—. 2025, A&A, 693, A279, doi: 10.1051/0004-6361/202450953

Petroff, E., Hessels, J. W. T., & Lorimer, D. R. 2022, A&A Rv, 30, 2, doi: 10.1007/s00159-022-00139-w

Ravi, V. 2019, Nature Astronomy, 3, 928, doi: 10.1038/s41550-019-0831-y

Smirnov, N. 1948, Annals of Mathematical Statistics, 19, 279

Spitler, L. G., Scholz, P., Hessels, J. W. T., et al. 2016, Nature, 531, 202, doi: 10.1038/nature17168

Wang, W., Zhang, B., Chen, X., & Xu, R. 2019, ApJL, 876, L15, doi: 10.3847/2041-8213/ab1aab

Yamasaki, S., Goto, T., Ling, C.-T., & Hashimoto, T. 2024, MNRAS, 527, 11158, doi: 10.1093/mnras/stad3844

Yao, J. M., Manchester, R. N., & Wang, N. 2017, ApJ, 835, 29, doi: 10.3847/1538-4357/835/1/29

Zhang, B. 2018, ApJL, 867, L21, doi: 10.3847/2041-8213/aae8e3

—. 2020, Nature, 587, 45, doi: 10.1038/s41586-020-2828-1

Zhang, L.-X., Tian, S., Shen, J., et al. 2025, arXiv e-prints, arXiv:2507.14711, doi: 10.48550/arXiv.2507.14711

Zhang, Y.-K., Wang, P., Feng, Y., et al. 2022, Research in Astronomy and Astrophysics, 22, 124002, doi: 10.1088/1674-4527/ac98f7

Zhang J.-S., Wang, T.-C., Wang, P., et al. 2025, arXiv e-prints, arXiv:2507.14707, doi: 10.48550/arXiv.2507.14707

Zhou, D. J., Han, J. L., Zhang, B., et al. 2022, Research in Astronomy and Astrophysics, 22, 124001, doi: 10.1088/1674-4527/ac98f8

Zhu, Y., Niu, C., Dai, S., et al. 2024, Chinese Physics Letters, 41, 109501, doi: 10.1088/0256-307X/41/10/109501

APPENDIX

Appendix Table A1. Properties of the multi-component burst-clusters (≥2-components).

Burst ID	Component	TOAs (MJD)@1.5 GHz	DM ($pc\,cm^{-3}$)	Center Freq (MHz)	Bottom Freq (MHz)	Top Freq (MHz)
B88	1	59172.20155284418433	1201.3(0.1)	1439.596752	1411.179314	1468.014189
B89	2	59172.20155299289763	1201.3(0.1)	1444.22042	1374.40458	1499.87793
B91	1	59208.08742101160169	1195.7(0.1)	1445.429289	1382.781953	1499.87793
B92	2	59208.08742137546506	1195.7(0.1)	1429.833983	1342.71176	1499.87793
B104	1	59208.11264542803110	1193.2(0.2)	1440.03506	1385.75797	1494.31214
B105	2	59208.11264683925401	1193.2(0.2)	1415.413442	1388.229317	1442.597568
B116	1	59224.04922651168454	1198.2(0.1)	1453.823954	1340.785357	1499.87793
B117	2	59224.04922798402549	1198.2(0.1)	1418.567731	1332.101247	1499.87793
B134	1	59306.82174683937774	1194.1(0.1)	1393.457246	1304.941428	1481.973063
B135	2	59306.82174697117443	1194.1(0.1)	1392.749582	1316.966929	1468.532235
B140	1	59306.83829678239999	1194.0(0.1)	1413.714683	1364.411655	1463.017712
B141	2	59306.83829764356051	1194.0(0.1)	1371.266031	1232.997796	1499.87793
B152	1	59347.73112721699727	1205.2(0.7)	1448.46554	1408.07488	1488.8562
B153	2	59347.73112785528065	1205.2(0.7)	1392.14125	1326.61413	1457.66838
B154	1	59355.70649803764536	1196.9(0.2)	1379.74938	1320.75878	1438.739981
B155	2	59355.70649877208052	1196.9(0.2)	1359.894877	1284.168482	1435.621271
B159	1	59475.37105939972389	1190.4(0.1)	1408.092101	1307.478778	1499.87793
B160	2	59475.37105984813388	1190.4(0.1)	1339.230423	1287.136193	1391.324653
B161	1	59475.38309604497044	1191.4(0.2)	1447.197391	1376.314962	1499.87793
B162	2	59475.38309652624594	1191.4(0.2)	1447.197391	1376.314962	1499.87793
B178	1	59554.15544217405113	1184.8(0.1)	1441.920893	1361.395049	1499.87793
B179	2	59554.15544230146770	1184.8(0.1)	1360.228531	1228.823934	1491.633128
B189	1	59560.16473174953717	1183.8(0.1)	1488.30718	1404.33824	1499.87793
B190	2	59560.16473193652928	1183.8(0.1)	1386.329255	1238.535024	1499.87793
B191	3	59560.16473212611891	1183.8(0.1)	1382.744672	1278.593328	1486.896016
B192	4	59560.16473236353340	1183.8(0.1)	1398.097429	1303.922838	1492.27202
B209	1	59580.08211609908903	1180.7(0.1)	1475.632947	1417.787545	1499.87793
B210	2	59580.08211673732876	1180.7(0.1)	1368.759931	1252.668636	1484.851225
B211	1	59580.08666774126323	1182.8(0.2)	1357.036045	1282.381258	1431.690833
B212	2	59580.08666789661947	1182.8(0.2)	1417.081412	1376.023966	1458.138859
B219	1	59604.00552298274852	1185.0(0.1)	1215.353104	1133.863568	1296.842639
B220	2	59604.00552331320068	1185.0(0.1)	1242.040473	1143.58	1340.500946
B221	3	59604.00552347524354	1185.0(0.1)	1301.10519	1171.495354	1430.715025
B229	1	59632.93453996753669	1194.3(0.1)	1420.368541	1325.873149	1499.87793
B230	2	59632.93454041893710	1194.3(0.1)	1447.96008	1426.09629	1469.82387
B231	3	59632.93454092050524	1194.3(0.1)	1219.488262	1160.218376	1278.758148
B233	1	59641.92190177011798	1185.0(0.0)	1421.9542	1361.72358	1482.18482
B234	2	59641.92190313873289	1185.0(0.0)	1421.13769	1323.59275	1499.87793
B252	1	59671.82928816841741	1180.6(0.2)	1245.522078	1136.090558	1354.953599
B253	2	59671.82928860051470	1180.6(0.2)	1134.2553	1087.83086	1180.67974
B258	1	59671.85351685265050	1178.0(0.1)	1436.581926	1342.090273	1499.87793

B259	2	59671.85351746199740	1178.0(0.1)	1448.52009	1405.302996	1491.737183
B261	1	59671.85659109426342	1176.2(0.2)	1263.827493	1184.583878	1343.071107
B262	2	59671.86551290835632	1176.2(0.2)	1246.42978	1169.119366	1323.740194
B263	1	59671.86299286691064	1181.1(0.1)	1350.610982	1287.639805	1413.582159
B264	2	59671.86299317443627	1181.1(0.1)	1357.75772	1295.977996	1419.537445
B265	3	59671.86299358931137	1181.1(0.1)	1209.754147	1000	1438.069033
B267	1	59671.86551252580102	1184.3(0.2)	1324.79933	1238.78023	1410.98673
B268	2	59672.82162277348107	1184.3(0.2)	1091.97256	1000	1186.70003
B284	1	59673.85253208376525	1186.5(0.1)	1261.634547	1193.052185	1330.216909
B285	2	59673.85253500939143	1186.5(0.1)	1345.162549	1235.393067	1454.932032
B301	1	59705.75039521722647	1187.7(0.1)	1370.16629	1347.01602	1393.31656
B302	2	59705.75039591296081	1187.7(0.1)	1450.188561	1430.261616	1470.115507
B308	1	59747.64526278508856	1183.0(0.1)	1385.97266	1323.75721	1448.18811
B309	2	59747.64526328403008	1183.0(0.1)	1444.54027	1397.67329	1491.40724
B328	1	59820.43713358692185	1172.8(0.1)	1386.205173	1306.050971	1466.359375
B329	2	59820.43713382320857	1172.8(0.1)	1295.904172	1224.263213	1367.54513
B343	1	59839.38941793060076	1164.5(0.1)	1428.233911	1369.898468	1486.569353
B344	2	59839.38941815464932	1164.5(0.1)	1427.561852	1380.977244	1474.146461
B348	1	59852.33670939735021	1162.2(0.3)	1422.930849	1362.013439	1483.84826
B349	2	59852.33671153239993	1162.2(0.3)	1320.748105	1200.447395	1441.048814
B352	1	59871.30124151545169	1176.4(0.1)	1322.34169	1300.34506	1344.33832
B353	2	59871.30124189160415	1176.4(0.1)	1338.116295	1250.127555	1426.105036
B361	1	59894.21710628105211	1162.8(0.2)	1417.477493	1364.383841	1470.571145
B362	2	59894.21710658693337	1162.8(0.2)	1419.411757	1372.745718	1466.077797
B373	1	59910.16238363894081	1169.1(0.0)	1277.417033	1118.077015	1436.75705
B374	2	59910.16239624022273	1169.1(0.0)	1417.505606	1372.177468	1462.833743
B376	1	59910.16408148084884	1179.5(0.1)	1416.42458	1341.516099	1491.333061
B377	2	59910.16408181364386	1179.5(0.1)	1426.596673	1329.984854	1499.87793
B379	1	59910.16880359954666	1172.7(0.1)	1452.655465	1383.047263	1499.87793
B380	2	59910.16880368578859	1172.7(0.1)	1428.3993	1373.070936	1483.727665
B384	1	59910.17863870527799	1179.3(0.1)	1465.37969	1403.50529	1500
B385	2	59910.17863917985960	1179.3(0.1)	1305.5432	1226.72705	1384.35934
B410	1	59960.06469329555694	1177.9(0.1)	1446.11881	1409.30689	1482.93073
B411	2	59960.06469358679897	1177.9(0.1)	1448.65169	1406.49364	1490.80974
B413	1	59960.06738932633743	1181.8(0.1)	1428.316426	1389.341124	1467.291727
B414	2	59960.06738956437766	1181.8(0.1)	1346.340465	1248.203413	1444.477516
B421	1	59987.95267183618125	1171.9(0.1)	1330.643188	1248.401412	1412.884963
B422	2	59987.95267201295064	1171.9(0.1)	1275.814435	1203.131564	1348.497306

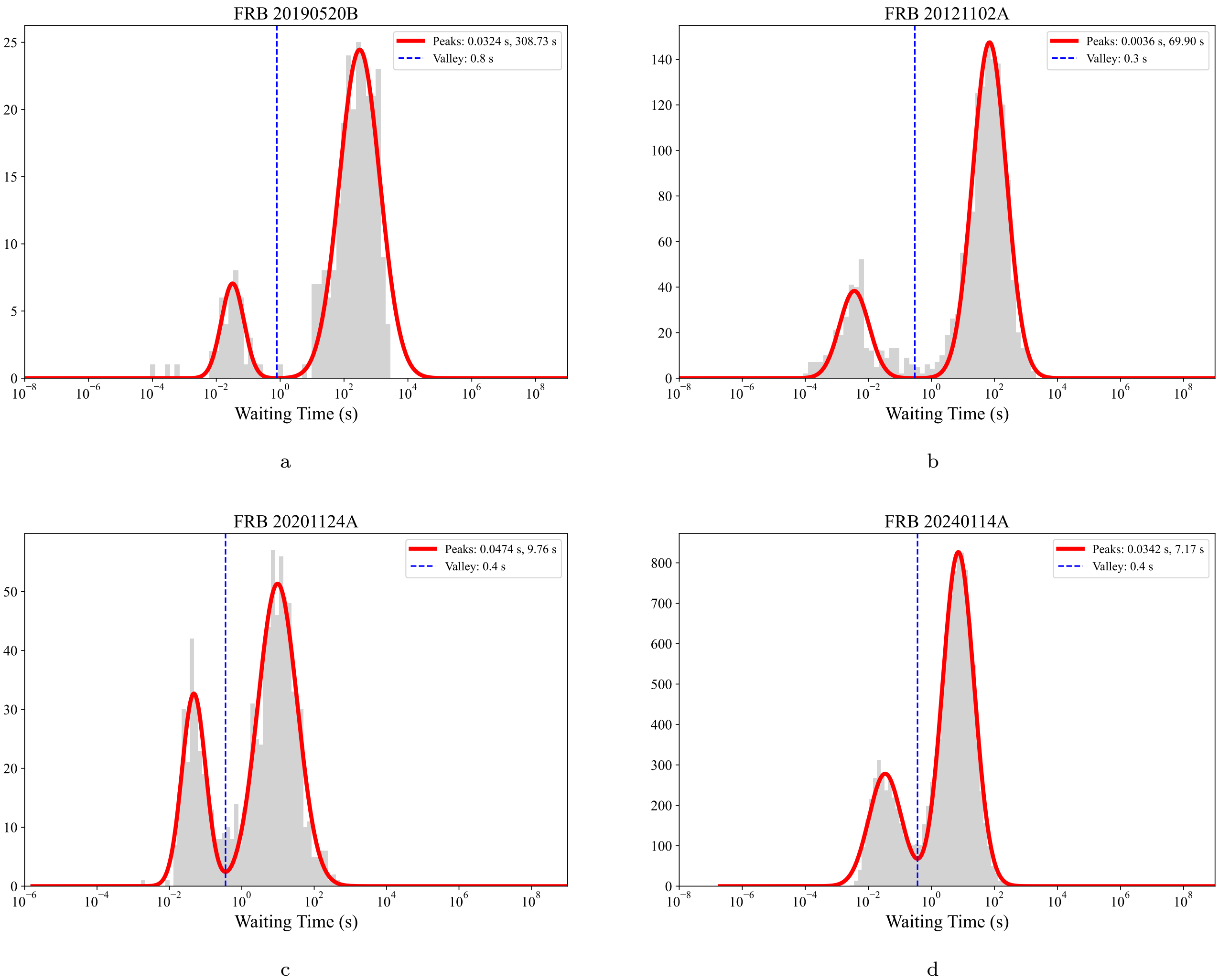

Appendix Figure A1. Waiting time distribution of four FRBs. The histogram shows the waiting time distribution, with the red line representing the lognormal double-peak fit. The two peaks correspond to the characteristic waiting times, with their values labeled in the upper right corner of the plot. The blue dashed line marks the valley between the peaks, and the valley time is used as a criterion to distinguish whether the events belong to a single burst-cluster.

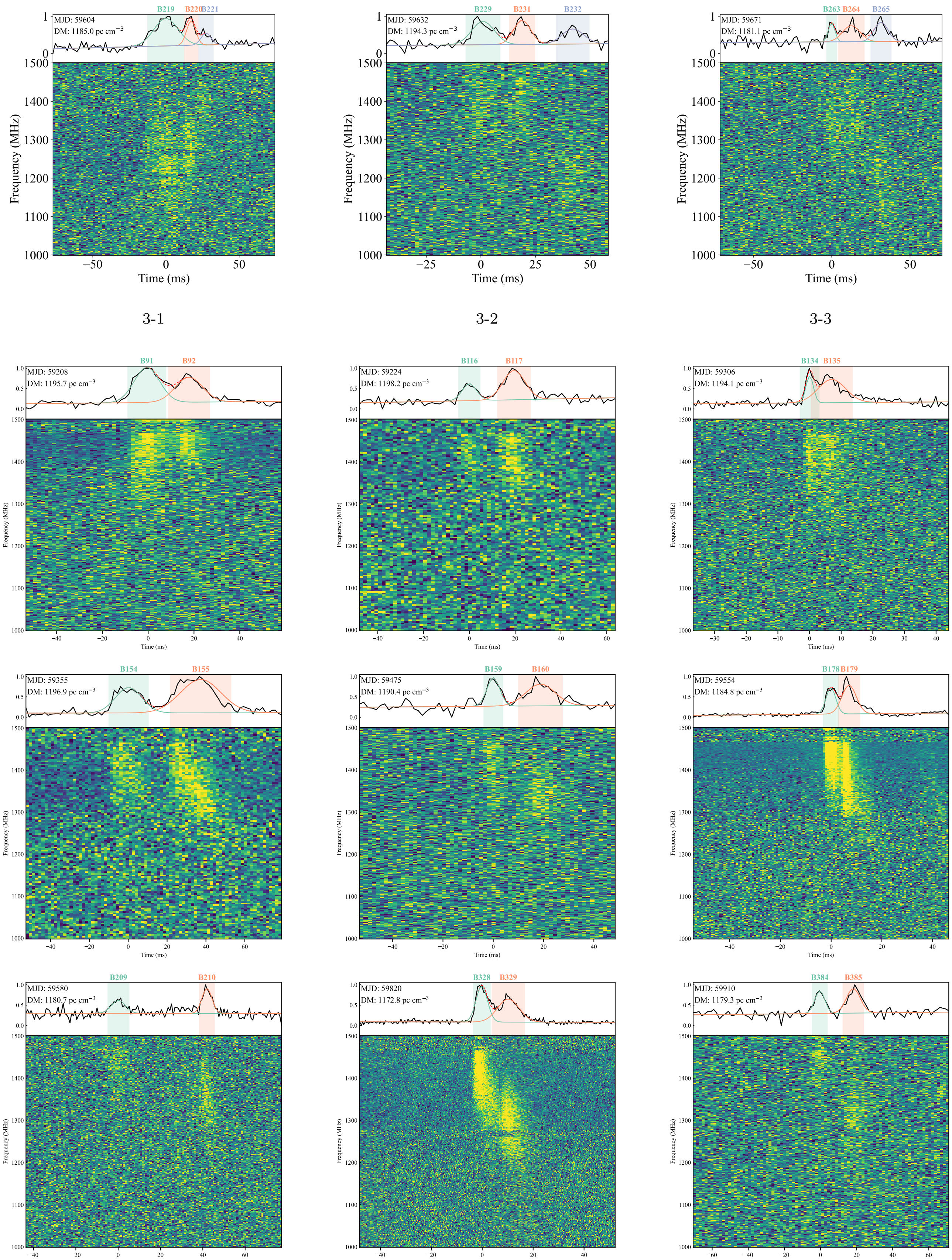

Appendix Figure A2. Two-dimensional dynamic spectra of multi-component burst-clusters from FRB 20190520B. The top row presents a three-component burst-cluster, while the following three rows display nine representative two-component burst-clusters. The three-component burst-cluster is labeled with indices 3-1, 3-2, and 3-3 beneath each panel. The presentation follows the same format as Figure 4.

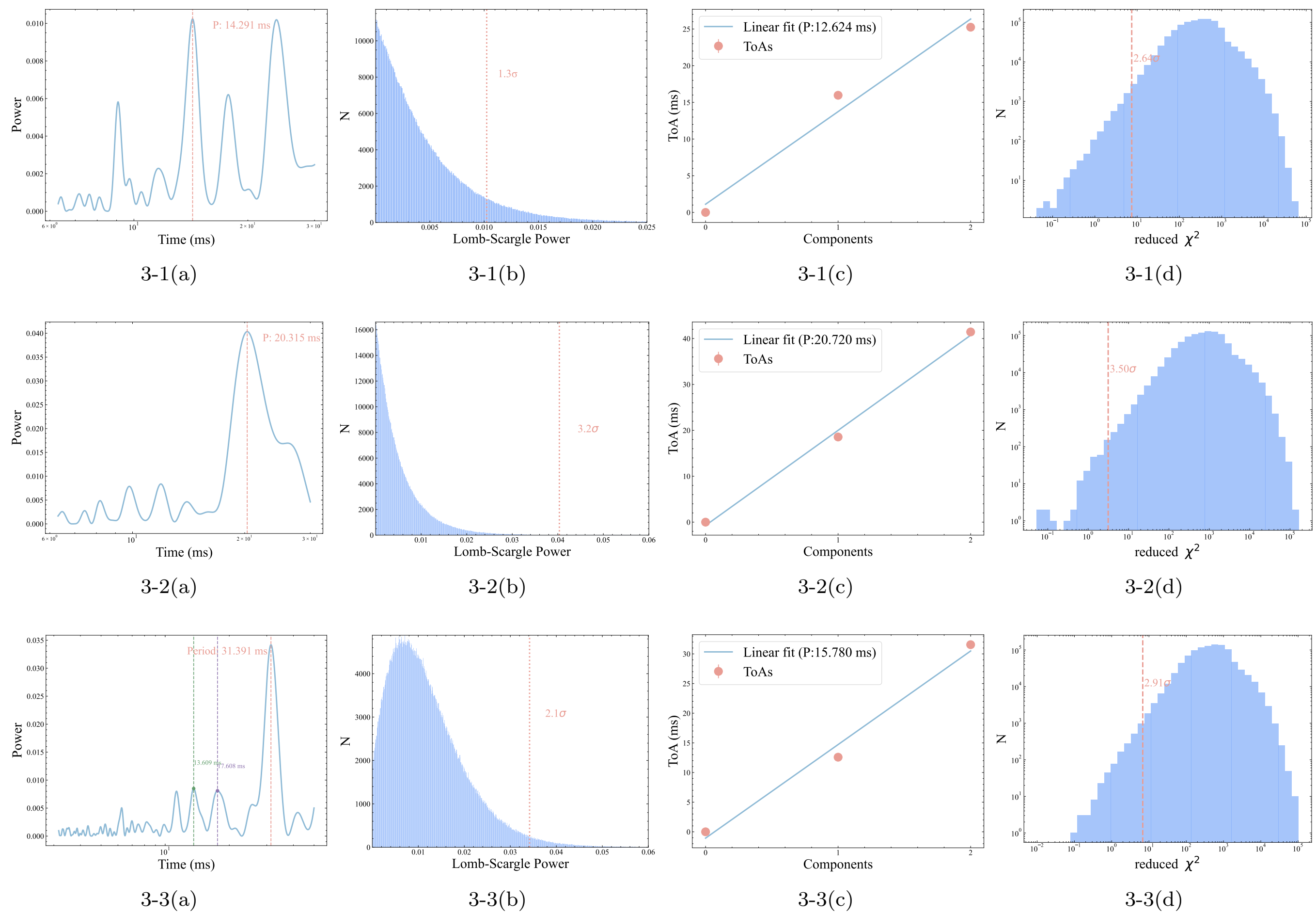

Appendix Figure A3. Temporal analysis of the three-component burst-cluster. Panels labeled as 3-1(a)–3-1(d), 3-2(a)–3-2(d), and 3-3(a)–3-3(d) correspond to the periodicity search results of the sub-panels 3-1, 3-2, and 3-3 in Appendix Figure A2, respectively. The presentation follows the same format as Figure 5. For the 3-3 case, panels (a) and (b) show distinct behavior: in panel (a), the highest Lomb–Scargle power corresponds to the time separation between the first and third peaks, rather than the expected adjacent spacing. This arises because the first and third pulses are broader in width compared to the second pulse. The green and purple dashed lines mark the separations between peaks 1–2 and 2–3, respectively, for reference.